Environmental Science & Technology

Article

Cite This: Environ. Sci. Technol. 2019, 53, 13878−13887

pubs.acs.org/est

Tuning Electron Density Endows $Fe_{1-x}Co_xP$ with Exceptional Capability of Electrooxidation of Organic Pollutants

Haopeng Feng,[†,‡,∥] Jiangfang Yu,[†,‡,∥] Lin Tang,[*,†,‡] Guangming Zeng,[†,‡] Wangwang Tang,[†,‡] Jiajia Wang,[†,‡] Ting Luo,[†,‡] Bo Peng,[†,‡] Biao Song,[†,‡] Longlu Wang,[§] and Chao Liang[†,‡]

[†]College of Environmental Science and Engineering and [§]School of Physics and Electronics, Hunan University, Changsha 410082, China

[‡]Key Laboratory of Environmental Biology and Pollution Control (Hunan University), Ministry of Education, Hunan University, Changsha 410082, Hunan, China

Supporting Information

ABSTRACT: The good performance of base metal catalysts for the electrooxidation of organic pollutants has attracted great attention. However, base metal phosphides for electrooxidation are seldom studied owing to the sluggish water adsorption and dissociation dynamics, which will hinder the production of the sorbed hydroxyl radicals (M(•OH)) and thus inhibit the electrooxidation of organic pollutants. Herein, we proposed a universal strategy to improve the electrooxidation capability of metal phosphides by modulating the surface electron densities. The electron interactions between cobalt (Co) and phosphorus (P) are modulated after iron doping, resulting in more positively charged Co and more negatively charged P, which can promote the adsorption and activation of water molecules and produce large quantities of M(•OH). Meanwhile, the experimental results show that the iron-modulated $Fe_{0.53}Co_{0.47}P$ nanosheet arrays exhibit higher removal efficiency of tetracycline than the boron-doped diamond and Pt anode at low current intensity. Based on experimental results and density functional theory + U calculations (DFT + U), it is found that $Fe_{0.53}Co_{0.47}P$ has lower barrier (0.45 eV) to form the sorbed hydroxyl radicals (M(•OH)) and higher overpotential to produce O_2 than its counterparts, suggesting that $Fe_{0.53}Co_{0.47}P$ can produce more M(•OH) instead of O_2. The above results highlighted the feasibility of these base metal phosphides for electrooxidation for advanced water purification.

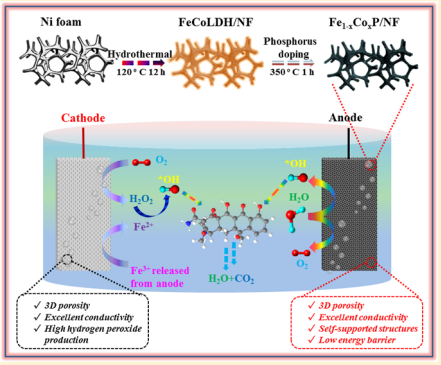

1. INTRODUCTION

Hundreds of rivers around the world are flooded with excessive doses of antibiotics.[1−3] Antibiotic contamination makes bacteria resistant to this life-saving drug. These drugs leak into rivers and soil from human and animal excreta, wastewater treatment plants, and pharmaceutical facilities. Antibiotic-resistant bacteria can be found in many different environments. This will threaten human health and ecological balance. Common antibiotics can be divided into tetracycline, aminoglycoside, quinolone, macrolide, and sulfonamide based on their chemical structures. Among them, tetracycline is reported to be one of the most widely used antibiotics. Although the concentration of tetracycline in natural water is relatively low, the pollutant is highly resistant to biological treatment.[4,5] Thus, it is essential to find an economical and efficient technique to solve the problem of tetracycline contamination.

Electrooxidation as one of the most popular electrochemical advanced oxidation processes can efficiently oxidize organic pollutants.[6] It can produce hydroxyl radicals (•OH) on the surface of the anode material (defined as M) by the water oxidation reaction (eq 1). The sorbed hydroxyl radical M(•OH) is a nonselective oxidant with high activity for organic pollutants, and it can degrade organic pollutants until the ultimate oxidation state is reached (eq 2).[7] This process is considered to be one of the most effective techniques for the purification of wastewater with low concentrations of recalcitrant organic pollutants.[8] Boron-doped diamond (BDD) electrodes are known as the best anode material for electrooxidation because they have high chemical stability and can produce large quantities of M(•OH) (defined as •OH adsorbed on the anode material), which can completely mineralize organic pollutants.[9] However, the high cost and scarcity limit their large-scale application.[10] Therefore, it is essential to fabricate base metal electrocatalysts with high activity and good durability for electrooxidation.

$$M + H_2O \rightarrow M(^{\cdot}OH) + H^+ + e^- \quad (1)$$

$$M(^{\bullet}OH) + \text{organics} \rightarrow M + CO_2 + H_2O + \text{inorganic ions} \quad (2)$$

Received: August 11, 2019
Revised: November 4, 2019
Accepted: November 7, 2019
Published: November 7, 2019

DOI: 10.1021/acs.est.9b04859
Environ. Sci. Technol. 2019, 53, 13878−13887

Cobalt phosphide (CoP) has attracted considerable attention because of its excellent electrical conductivity, hybrid d orbitals, and versatile redox nature.[11−17] Unfortunately, the electrooxidation of organic pollutants by CoP is inactive in acidic aqueous solutions because of the sluggish water adsorption and dissociation dynamics, which is essentially determined by its inherent structural nature.[18] Although the morphological engineering can improve the electrooxidation ability of metal phosphides to a certain extent by increasing the catalytic sites, it cannot essentially change the intrinsic catalytic nature of metal phosphides. Recently, some researchers have found that the oxygen evolution reaction (OER) activities of the metal phosphides can be improved through the introduction of other promoter species to form binary phosphides. For example, Liang and co-workers doped Ni into CoP to form NiCoP nanomaterials and the electrocatalyst exhibited highly catalytic activity and long-term durability toward OER.[19] In addition, Zhang et al. reported that Fe-doped NiP nanosheets as highly stable electrocatalysts for OER showed a low overpotential of 182 mV at 100 mA cm^{-2}.[20] The electrooxidation and OER process have many similarities. Although the byproduct O_2 will be produced during the process of electrooxidation of organic pollutants and leads to a decrease in the efficiency of current utilization, it can be avoided by selecting appropriate electrode materials and potential. Therefore, we firmly believe that the electrooxidation ability of metal phosphides can be improved by doping other metal elements appropriately. It can produce more M($^{\bullet}$OH) instead of O_2 by appropriately regulating and controlling the molar ratio of two different metals. Moreover, the understanding of the essences of electrooxidation of organic pollutants under acidic conditions, especially at atomic levels, is absent. Consequently, promoting the electrooxidation capability of metal phosphides by rationally regulating the electronic density of catalytic sites and unraveling the essences of modulation mechanism is highly desired but challenging. Besides, the binder-free self-supported electrocatalysts grown directly on substrates can improve the intrinsic activity and kinetics of electrooxidation through accelerating electron transfer from electron-conductive substrate to electrocatalysts. Therefore, it is worthwhile to design a self-supported electrocatalyst for the electrooxidation process.

Here, we propose a facile and universal strategy to modulate the electron densities of the catalytic sites of $Fe_{1-x}Co_xP$ nanosheet arrays on three-dimensional Ni-foam (NF) for efficient electrooxidation and degradation of organic pollutants by using iron as the modulator. The design principle is to increase the positive charge of metal sites by iron incorporation, which is conducive to adsorbing water molecules and promoting H−O cleavage. The Fe-modulated $Fe_{1-x}Co_xP$ exhibits high electrooxidation ability and stability in acidic media. The characterization methods, experimental results, and density functional theory + U (DFT + U) calculations further demonstrate that the surface electron densities and d-band centers of $Fe_{1-x}Co_xP$ can be effectively modulated by Fe doping. The ability to manipulate the electron densities and d band centers of the catalytic sites through rational surface engineering can offer a new insight for the development of highly efficient electrooxidation catalysts beyond.

2. MATERIALS AND METHODS

2.1. Material Synthesis. *2.1.1. Synthesis of $Fe_{1-x}Co_x$-LDH/NF.* A piece of NF (40 × 20 × 1.0 mm, 300 g m^{-2}, LiZhi Yuan, Taiyuan, China) was cleaned in acetone solution and HCl solution (3.0 M) with sonication for 10 min, respectively, and subsequently washed thoroughly with ethanol and deionized water. $Fe_{1-x}Co_x$-LDH arrays with different Fe/Co ratios (e.g., 0/1, 0.29/0.71, 0.57/0.43, 0.71/0.29, 1/0) were grown on NF by a simple hydrothermal process. First, 8 mmol of NH_4F, 10 mmol of urea, and 1.4 mmol of metal salt ($Fe(NO_3)_3{\cdot}9H_2O$ and $Co(NO_3)_2{\cdot}6H_2O$) with different molar ratios of Fe/Co were dissolved in 40 mL of deionized water to form a homogeneous solution. Then, the pretreated NF was immersed in an 80 mL Teflon-lined stainless-steel autoclave containing the above solution, sealed, and maintained at 120 °C for 12 h. After natural cooling, the NF loaded with $Fe_{1-x}Co_x$-LDH arrays was taken out and then washed with deionized water and ethanol. Finally, it was dried at 60 °C under vacuum, and the mass loading of $Fe_{1-x}Co_x$-LDH/NF is ∼5 mg cm^{-2}. All chemicals were of analytical grade.

2.1.2. Phosphorization of $Fe_{1-x}Co_x$-LDH/NF. The prepared $Fe_{1-x}Co_x$-LDH/NF and NaH_2PO_2 powder (1.0 g) were placed, respectively, in two opposite positions of the tube furnace in two quartz boats with the phosphorus source at the upstream side. Then, they were heated to 350 °C with a ramp rate of 2 °C min^{-1} and held at this temperature for 60 min under the N_2 atmosphere. The mass loading values of the $Fe_{1-x}Co_xP$ catalysts are shown in Table S2.

2.2. Characterizations. The component and morphology of electrocatalysts were characterized with energy-dispersive X-ray spectroscopy (EDX) and scanning electron microscopy (SEM). Transmission electron microscopy (TEM) and high-resolution TEM (HRTEM) images were taken by a JEOL-2100F electron microscope operated at 200 kV. X-ray diffraction (XRD) was obtained on a Bruker D8 Advance X-ray diffractometer (Cu Kα radiation, λ = 1.54178 Å). X-ray photoelectron spectroscopy (XPS) spectra were recorded with a Kratos ASIS-HS X-ray photoelectron spectroscope (15 kV, 10 mA). The element content was determined by inductively coupled plasma mass spectrometry (ICP-MS, Thermo Scientific iCAP6300) analysis.

2.3. Electrochemical Measurements. The electrooxidation experiments were conducted in an open electrolytic cell containing the prepared $Fe_{1-x}Co_xP$/NF anode and a carbon felt cathode (30 × 20 × 5.0 mm). An aqueous solution (200 mL) of 70 mg L^{-1} tetracycline hydrochloride containing 0.05 M Na_2SO_4 as the electrolyte was performed to conduct the electrooxidation experiments under different constant current densities (6.25 and 12.5 mA cm^{-2}) at pH 5, and the air was not bubbled into the system during the whole reaction process. All tests for kinetics experiments and mineralization of contaminants in solutions were conducted under natural condition and sampled in triplicate. The mean values with an error < 1.8% are shown in the figures. The samples are filtered with a 0.45 μm filter, and it has been demonstrated to have no intercepting effects for the tetracycline molecules. Then, the samples are analyzed by the UV−vis absorbance at 357 nm.

The electrocatalytic performances of as-prepared electrode materials were tested in a three-electrode system. $Fe_{1-x}Co_xM$/NF was used as the working electrode. A carbon rod and an Ag/AgCl electrode were used as the counter electrode and the reference electrode, respectively. Prior to recording the

DOI: 10.1021/acs.est.9b04859
Environ. Sci. Technol. 2019, 53, 13878−13887

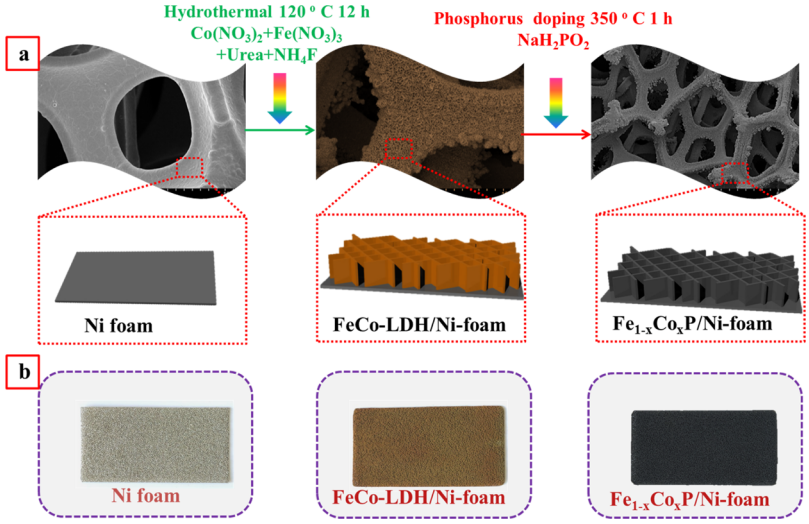

Figure 1. (a) Schematic illustration of the two-step method for synthesizing 3D network FeCo-LDH/NF and $Fe_{1-x}Co_xP$/NF electrodes and (b) optical images of initial NF, as-prepared FeCo-LDH/NF, and $Fe_{1-x}Co_xP$/NF, respectively.

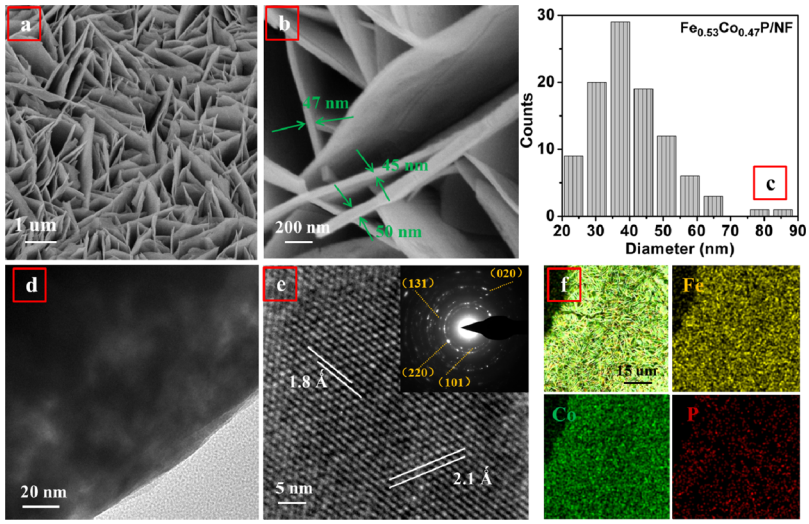

Figure 2. (a,b) SEM images of $Fe_{0.53}Co_{0.47}P$/NF, (c) distribution histograms of the thickness of $Fe_{0.53}Co_{0.47}P$/NF, (d) TEM images of pure $Fe_{0.53}Co_{0.47}P$ compound, (e) HRTEM image and inset of the SAED pattern taken from the $Fe_{0.53}Co_{0.47}P$ nanosheet, and (f) SEM image and EDS element mapping of Fe, Co, and P for the $Fe_{0.53}Co_{0.47}P$ nanosheet.

polarization curves, all prepared electrodes were activated by the cyclic voltammetry test at 10 mV s^{-1}. All voltages and potentials were *iR*-corrected unless otherwise specified. Polarization curves were obtained using linear sweep voltammetry (LSV) curves at a scan rate of 5 mV s^{-1}. Electrochemical impedance spectroscopy (EIS) was performed at −0.30 V versus reversible hydrogen electrode (RHE) from 100 kHz to 0.1 Hz. All the potentials were measured against RHE.

2.4. Structural Optimization. All calculations in this study were performed using the Vienna ab initio simulation package.[21,22] We used the Perdew−Burke−Ernzerhof functional for the projector augmented wave potential[23,24] and exchange−correlation energy.[25] The kinetic energy cutoff was set to 400 eV. The *k*-point meshes were sampled based on the Gaussian method. To minimize the undesired interactions between images, a vacuum of at least 15 Å was considered along the *z* axis. DFT simulations performed were based on the experimental crystal structure of CoP[6] (*a* = 5.077 Å, *b* = 3.281 Å, *c* = 5.587 Å, ICSD collection code # 43249). The structures of $Fe_{0.25}Co_{0.75}P$ and $Fe_{0.5}Co_{0.5}P$ were obtained by substituting the cobalt atom within the unit cell with Fe atoms in all possible geometries and selecting the most stable ones. Chemisorption was modeled on the CoP, $Fe_{0.25}Co_{0.75}P$, and $Fe_{0.5}Co_{0.5}P$ (101) surfaces. The surfaces were constructed as the slab consisting of three layers within periodic boundary conditions, separated by a 20 Å vacuum layer. For these calculations, three layers with a 2 × 2 × 1 *k*-point mesh were used in the 2 × 2 super cells for CoP, $Fe_{0.25}Co_{0.75}P$, and $Fe_{0.5}Co_{0.5}P$.

3. RESULTS AND DISCUSSION

3.1. Structural and Compositional Characterization of $Fe_{1-x}Co_xP$/NF. The schematic diagram shows the prepared process of the three-dimensional (3D) $Fe_{1-x}Co_xP$ arrays on NF substrates (Figure 1a). A range of $Fe_{1-x}Co_x$ layered double hydroxide ($Fe_{1-x}Co_x$-LDH) arrays with diverse Fe/Co molar ratio are grown on NF by a simple hydrothermal process. It

DOI: 10.1021/acs.est.9b04859
Environ. Sci. Technol. 2019, 53, 13878−13887

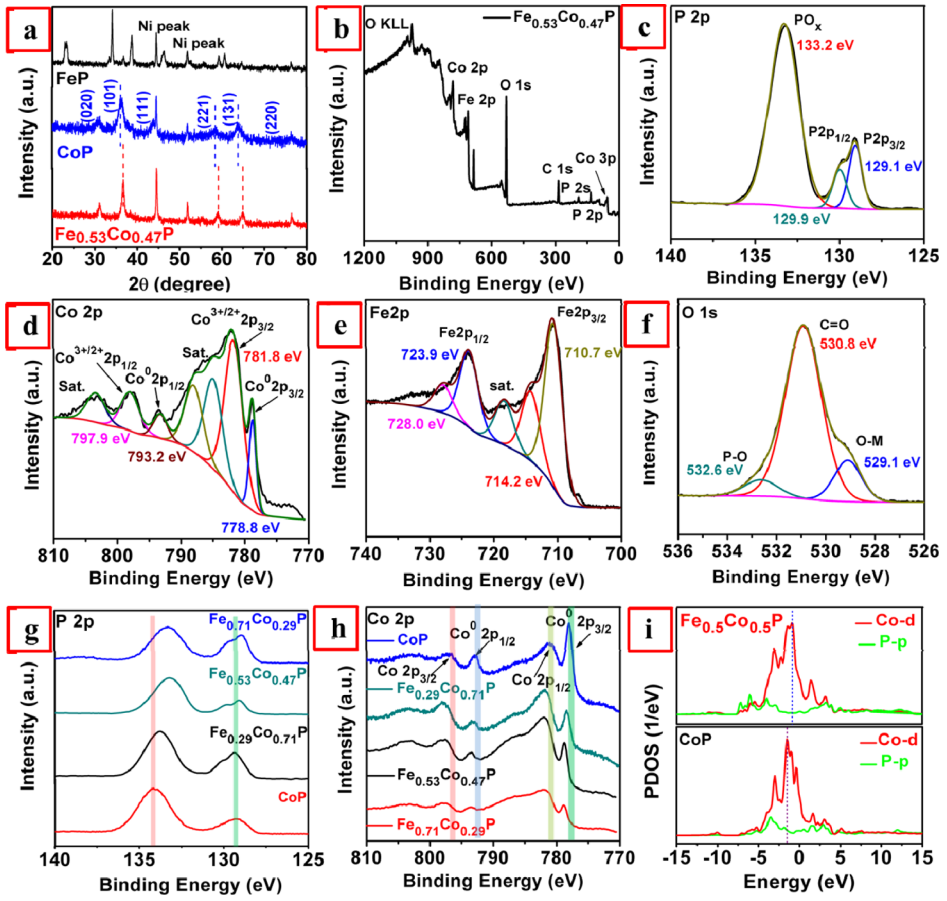

Figure 3. (a) XRD images of FeP, CoP, and $Fe_{0.53}Co_{0.47}P$; (b) high-resolution specific region XPS spectra for $Fe_{0.53}Co_{0.47}P$ high-resolution specific region XPS spectra of CoP, $Fe_{0.29}Co_{0.71}P$, $Fe_{0.53}Co_{0.47}P$, and $Fe_{0.71}Co_{0.29}P$ in (c) Co 2p, (d) P 2p; and high-resolution specific region XPS spectra of $Fe_{0.53}Co_{0.47}P$ in (f) P 2p, (g) Fe 2p, (h) O 1s, and (i) calculated PDOS of CoP and $Fe_{0.5}Co_{0.5}P$ (d): Co 3d orbitals and P p-orbitals.

can be clearly observed that $Fe_{1-x}Co_x$-LDH with a nanosheet structure is evenly covered on the smooth NF (Figures S1 and S2). NF is often used as the substrate because it possesses macropores and a 3D conductive network. Different color $Fe_{1-x}Co_x$-LDHs are obtained on NF because of the different content of Fe doping after the hydrothermal process (Figure S3a). The $Fe_{1-x}Co_x$-LDH nanosheet arrays with a Fe/Co molar ratio of 0.53/0.47 (defined as $Fe_{0.53}Co_{0.47}$-LDH/NF) are interconnected and vertically grown on the NF framework, which will increase the contact area between the catalyst and electrolyte. There is no doubt that it will speed up the electron transfer between reactants. Then, $Fe_{1-x}Co_xP$/NFs are obtained by one-step heat treatment in the PH_3 atmosphere at 350 °C for 60 min. The color of the sample turns black after phosphating, which proves that $Fe_{0.53}Co_{0.47}$-LDH/NF has been successfully converted into $Fe_{0.53}Co_{0.47}P$/NF (Figure 1b and Figure S3b). From Figure 2a, it shows the uniform overlap of the $Fe_{0.53}Co_{0.47}P$/NF nanosheet arrays with a rough surface. The catalyst is roughened and deformed, but $Fe_{0.53}Co_{0.47}P$/NF still retains the nanosheet structure by topological transformation of FeCo-LDH/NF after phosphorization. Meanwhile, it can also be observed that the thickness of $Fe_{0.53}Co_{0.47}P$/NF nanosheet arrays is obviously reduced from 80−120 to 30−50 nm after phosphorization (Figures 2b,c and S2d). It is interesting to note that the morphology of CoP/NF has been changed from "flower-like" to nanosheet arrays with the doping of iron (Figures S4−S7). The EDX spectroscopy analysis was also used to determine the atomic ratios of Fe and Co in $Fe_{1-x}Co_xP$/NF, where the obtained Fe/Co ratio is approximate to the mole ratio of original materials (Table S1). The peak of nickel can be found in Figure S8. This is because the catalyst used for characterization was scratched from the NF loaded with the catalyst. Thus, the existence of metallic nickel particles in the sample is inevitable. The same phenomenon will also be found in the following XRD data. The XRD patterns of the bare CoP, FeP, and $Fe_{0.53}Co_{0.47}P$ are measured to study their crystal structures (Figure 3a). The result shows that the diffraction peaks of $Fe_{0.53}Co_{0.47}P$ move slightly to higher angles compared to that of CoP because the fringe lattice distances of the CoP crystalline lattice are altered by the incorporated Fe atoms because of the disparity in the atomic radii of Co and Fe. The peaks of nickel are also clearly found at 44.5 and 51.8°. This is consistent with the EDX data. The TEM images exhibit a sheetlike morphology of $Fe_{0.53}Co_{0.47}P$. It can also be found that there is a layer of an amorphous compound around the material, which can prevent the inner $Fe_{0.53}Co_{0.47}P$ from being corroded to some degree and improve the electrocatalytic performance by promoting the electron transfer between the inner metallic $Fe_{0.53}Co_{0.47}P$ and the outer layer (Figure S9).[26−28] The distinct particles can be seen in TEM images because of the existence of nickel particles. To eliminate the interference of nickel particles, pure $Fe_{0.53}Co_{0.47}P$ composite was synthesized without adding NF, and the result shows that no distinct nickel particles are found (Figure 2d). The clear lattice fringes with spacings of 2.1 and 1.8 Å can readily correspond to the (220) and (111) crystal

DOI: 10.1021/acs.est.9b04859
Environ. Sci. Technol. 2019, 53, 13878−13887

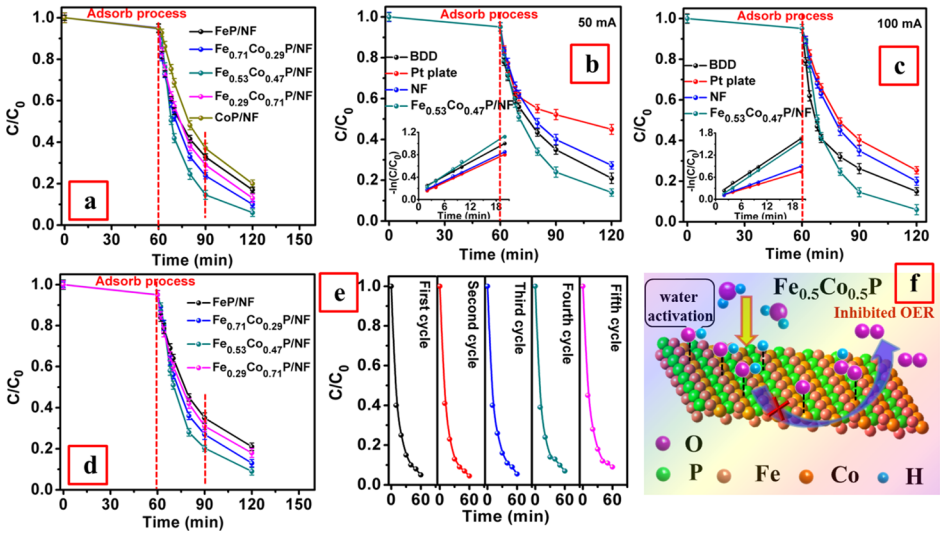

Figure 4. (a) Degradation efficiency of tetracycline by the $Fe_{1-x}Co_xP$/NF anode (pH = 5), effect of applied current on different anode materials (b) 50 mA and (c) 100 mA, (d) degradation efficiency of tetracycline by $Fe_{1-x}Co_xP$/NF in the presence of 1,10-phenanthroline, and (e) recyclability of $Fe_{0.53}Co_{0.47}P$/NF for the removal of tetracycline (pH = 5). (f) Schematic illustration of water adsorption, water activation, and oxygen generation processes.

planes of the $Fe_{0.53}Co_{0.47}P$ phase, respectively, which further proves the generation of crystalline $Fe_{0.53}Co_{0.47}P$ (Figure 2e). Furthermore, the selected area electron diffraction (SAED) pattern of $Fe_{0.53}Co_{0.47}P$ reveals the polycrystalline nature of the $Fe_{0.53}Co_{0.47}P$ nanosheet (inset in Figure 2e) and the elemental mapping further illustrates the homogeneous distribution of Co, Fe, and P elements on the whole nanosheet (Figure 2f). These results demonstrate that the $Fe_{0.53}Co_{0.47}P$/NF nanosheet arrays are successfully synthesized.

XPS is used for determining the surface composition and oxidation state of $Fe_{0.53}Co_{0.47}P$, and the results further confirmed the existence of Co, Fe, and P elements in the $Fe_{0.53}Co_{0.47}P$ nanosheet (Figure 3b). As shown in Figure 3c,d, the XPS spectra of P 2p can be deconvolved into three peaks that are located at 129.1 eV for P $2p_{3/2}$, 129.9 eV for P $2p_{1/2}$, and 133.2 eV for oxidized P species, respectively. In addition, two main peaks at 793.2 and 778.8 eV can be assigned to Co $2p_{1/2}$ and Co $2p_{2/3}$, respectively, which are regarded as Co^0. Meanwhile, the peak at 781.8 eV in the Co $2p_{3/2}$ region and that at 797.9 eV in the Co $2p_{1/2}$ region are regarded as oxidized Co species ($Co^{2+/3+}$). The other two peaks are satellite peaks.[29] The Fe 2p spectra show two spin orbital doublets at 723.9 and 714.2 eV corresponding to Fe^{3+} arising from the iron phosphate ($Fe-PO_x$), and the peaks at 718.0 and 710.7 eV are attributed to Fe^{2+} deriving from the Fe−P bonding structures (Figure 3e).[30,31] The fact that the characteristic peak of FeP is not observed in Fe 2p spectra indicates the existence of a ternary $Fe_{0.53}Co_{0.47}P$ compound instead of a mixture of two spin orbital phases.[32] The O 1s spectrum can be deconvolved into three peaks, including phosphorus−oxygen bond (532.6 eV), adventitious C═O functional group (530.8 eV), and metal−oxygen bond (529.1 eV) (Figure 3f).[33] To study the effect of iron doping on the electronic structure of materials, materials with different contents of iron doping are also tested. The peaks of Co 2p in $Fe_{1-x}Co_xP$ shift toward the high energy region after iron doping compared to that of Co 2p in CoP, and the peaks of P 2p in $Fe_{1-x}Co_xP$ shift toward the low energy region after iron doping compared to that of P 2p in CoP (Figures 3g−h and S10−S12). In other words, the binding energy of Co in $Fe_{1-x}Co_xP$ is positively shifted, and the binding energy of P is negatively shifted, indicating that the electronic structure of $Fe_{1-x}Co_xP$ has been changed, which may have great significance in improving the electrooxidation ability.[34]

To gain a better insight into the electronic structure adjustment of $Fe_{0.53}Co_{0.47}P$ with Fe doping, the partial density of states (PDOSs) of $Fe_{0.5}Co_{0.5}P$ (the Fe/Co ratio in the calculation model is similar to that in the experimental material $Fe_{0.53}Co_{0.47}P$) and pure CoP are calculated by theory calculation. To date, the band centers, band width, and overlapping are often used to discuss the multiple roles of electrocatalysts, including the catalytic activities, stabilities, and the properties of catalysts.[35,36] From Figure S13a, it can be observed that Fe 3d orbitals are bonded to Co 3d orbitals after Fe doping, suggesting a distinct electron transfer between Fe and Co atoms. Furthermore, the peak of Co 3d orbitals in $Fe_{0.5}Co_{0.5}P$ moved toward lower energy near the Fermi level compared to that of CoP in the PDOS images, which was consistent with the positive shift of the Co peak in XPS. It further demonstrates that the electronic structure of $Fe_{0.53}Co_{0.47}P$ with doped Fe has changed (Figure 3i). Proverbially, the Fermi level can evaluate the capacity of electron transfer on the catalysts surface. The high Fermi level value means the strong electron-transfer ability.[35,37] The Fermi level value of $Fe_{0.5}Co_{0.5}P$ (2.2 eV) is higher than that of CoP (1.6 eV), suggesting that iron doping can obviously enhance the electron-transfer ability of $Fe_{0.5}Co_{0.5}P$. This may improve the production of M(•OH) on the surface of the electrocatalyst. Meanwhile, the overlap of electronic clouds of Co in $Fe_{0.5}Co_{0.5}P$ is evidently enhanced compared to that of pure CoP (Figure S13b,c). The more overlap of electronic clouds implies a higher degree of electronic communication with a stronger metallicity. Moreover, the electron clouds gathered in the direction of doped atoms, suggesting an improved bonding capacity by doped Fe. It further demonstrates that the electronic structure of $Fe_{0.5}Co_{0.5}P$ with doped Fe was successfully tuned, and the charge density of Co in $Fe_{0.5}Co_{0.5}P$ obviously increased after iron doping because the

DOI: 10.1021/acs.est.9b04859
Environ. Sci. Technol. 2019, 53, 13878−13887

doping of iron will weaken the strength of the P−Co bond by generating the P−Fe bond, which makes Co atoms more positively charged and P atoms more negatively charged.[38] Considering that the water molecule is a polar molecule consisting of an O atom with negative charge and two H atoms with positive charge, the positively charged Co in $Fe_{0.5}Co_{0.5}P$ will adsorb and activate water molecules by capturing oxygen atoms. Therefore, $Fe_{0.5}Co_{0.5}P$ can efficiently improve water adsorption and activation and will thus accelerate the production of M(•OH).

3.2. Electrooxidation Performance of $Fe_{1-x}Co_xP$/NF. The kinetics of the degradation of tetracycline by anodic electrooxidation to produce oxidants (such as M(•OH)) are discussed based on the decay of tetracycline concentration. It is generally known that the applied current has tremendous influence on the degradation of the organic pollutant. However, the exorbitant current can inhibit the degradation efficiency because it will produce H_2O by $4e^-$ reduction instead of H_2O_2 on the surface of the cathode and generate O_2 instead of M(•OH) on the surface of the anode. Therefore, we adopted the low current to study the degradation process in this study. The results show that $Fe_{0.53}Co_{0.47}P$/NF exhibits the highest electrooxidation efficiency than its counterparts at the current density of 12.5 mA cm^{-2} (100 mA). As shown in Figure 4a, 94% of tetracycline is removed by $Fe_{0.53}Co_{0.47}P$/NF in only 60 min, while only 88, 85, 80.5, and 83% are achieved by $Fe_{0.71}Co_{0.29}P$/NF, $Fe_{0.29}Co_{0.71}P$/NF, CoP/NF, and FeP/NF, respectively. This is possibly because $Fe_{0.53}Co_{0.47}P$/NF has lower impedance and more active sites so that it can accelerate the adsorption and dissociation of water molecules. Therefore, the EIS measurements of $Fe_{1-x}Co_xP$/NF are performed at different potentials from 0.01 Hz to 10 kHz with an amplitude of 10 mV (Figure S14). The semicircles in the low- and high-frequency range of the Nyquist plot are attributed to the solution resistance and charge-transfer resistance (R_{ct}), respectively. The R_{ct} of $Fe_{0.53}Co_{0.47}P$/NF is much lower than those of CoP/NF, FeP/NF, and $Fe_{0.29}Co_{0.71}P$ under the overpotential of 100 mV. It means that $Fe_{0.53}Co_{0.47}P$/NF has faster electron-transfer ability. Meanwhile, the electrochemically active surface area (ECSA) is also used to evaluate the intrinsic activity of the $Fe_{1-x}Co_xP$/NF electrode. The area of all electrodes and the mass loading of catalysts on NF, such as $Fe_{0.53}Co_{0.47}P$/NF, $Fe_{0.29}Co_{0.71}P$, and CoP/NF, is almost the same (Table S2). Therefore, the improvement of electrooxidation performance may be attributed to the increase of ECSA. The ECSAs of FeP/NF, CoP/NF, $Fe_{0.71}Co_{0.29}P$, $Fe_{0.53}Co_{0.47}P$, and $Fe_{0.29}Co_{0.71}P$/NF are determined by the double-layer capacitance (C_{dl}) and calculated from C_{dl} (see the Supporting Information for details) (Figure S15).[35] Interestingly, the C_{dl} of $Fe_{0.53}Co_{0.47}P$/NF (65.6 mF cm^{-2}, 1640.0 cm_{ECSA}^2) is still larger than those of CoP/NF (34.27 mF cm^{-2}, 856.75 cm_{ECSA}^2), FeP/NF (17.6 mF cm^{-2}, 440.0 cm_{ECSA}^2), $Fe_{0.29}Co_{0.71}P$/NF (44.18 mF cm^{-2}, 1104.5.0 cm_{ECSA}^2), and $Fe_{0.71}Co_{0.29}P$/NF (52.5 mF cm^{-2}, 1312.5 cm_{ECSA}^2). It suggests that $Fe_{0.53}Co_{0.47}P$/NF has more electrochemical active sites. Therefore, the improved electrooxidation ability of $Fe_{0.53}Co_{0.47}P$/NF compared to its counterparts could be ascribed to large ECSAs and small electronic-/mass-transfer resistances. Meanwhile, the adsorption of tetracycline by anode materials and cathode materials is also considered, and the results show that the adsorption capacity for tetracycline is very low. The electrode is immersed in the reaction vessel for a period of time when switching on or off the power. From Figure 4a−d, it can be observed that only about 5% of tetracycline is removed by adsorption in 60 min, and about 8% of tetracycline is removed in 120 min (Figure S16a). However, the removal efficiency of tetracycline can reach nearly 95% after 60 min when the power is turned on. It demonstrates that the effect of adsorption on the removal of tetracycline is minimal in the electrooxidation process.

The comparison studies with other anode materials are carried out at the current densities of 6.25 mA cm^{-2} and 12.5 mA cm^{-2}, respectively. As shown in Figure 4b,c, the degradation rate and efficiency of tetracycline by the BDD anode are higher than those of the NF anode and Pt plate anode under the same experimental conditions. This is because the BDD anode possessed a higher overpotential for OER than NF and the Pt plate anode, which enabled it to produce more hydroxyl radicals. In addition, BDD(•OH) is physically adsorbed on the surface of the anode and easily oxidized to organics, while Ni(•OH) and Pt(•OH) are chemically adsorbed.[39,40] It can be observed that the $Fe_{0.53}Co_{0.47}P$/NF anode still exhibits higher electrooxidation efficiency than the BDD anode, especially at low applied current. Perhaps the reason is that it has a more appropriate overpotential, which can produce more M(•OH) and enhance the electrooxidation capability (reactions 1 and 2). Furthermore, the electro-generated H_2O_2 at the cathode by two electron reductions of oxygen can further react with Fe^{2+} released by $Fe_{0.53}Co_{0.47}P$/NF to generate homogeneous •OH (reactions 3 and 4). Apart from dissolved oxygen in the aqueous solution, the OER could also provide the required oxygen. It means that no additional oxygen donor is needed to provide O_2 in this system unlike other electro-fenton systems. There is no doubt that this system is more sustainable and energy-saving. To further reveal the effect of Fe^{2+} released from $Fe_{1-x}Co_xP$/NF, we compared the degradation efficiency of tetracycline by $Fe_{1-x}Co_xP$/NF with the 1,10-phenanthroline method. The results indicate that the removal efficiency of tetracycline slightly decreased when 1,10-phenanthroline is added to complex the soluble Fe^{2+} (Figure 4d). It demonstrates that the Fe^{2+} released by $Fe_{1-x}Co_xP$/NF can slightly improve the degradation efficiency of tetracycline by reacting with H_2O_2 to produce homogeneous •OH, but the removal efficiency of tetracycline by $Fe_{1-x}Co_xP$/NF is strongly relied on the electrooxidation process. The concentrations of Fe^{2+} released from $Fe_{1-x}Co_xP$/NF are determined in Figure S16b. The low concentrations of Fe^{2+} released from $Fe_{1-x}Co_xP$/NF also implied that $Fe_{1-x}Co_xP$/NF has excellent stability during the electrooxidation process. From Figure S17a, it can be observed that the concentration of H_2O_2 generated increased with the increase of current density. However, the faradaic efficiency (FE) (see the Supporting Information for details) for H_2O_2 production first increased and then decreased, reaching the maximum at 100 mA. The relatively low H_2O_2 FE is probably caused by the production of the H_2 byproduct as significant gas bubbles are observed (Figure S17c), especially under such a high current density.[41−43] The electrocatalytic hydrogen evolution reaction activity of the carbon felt is also tested, and the result shows that it needs 569 mV to reach the current density of 100 mA cm^{-2} (Figure S17b). This means that the cathode will produce not only H_2O_2 but also H_2 as a byproduct in the process of electrooxidation. Therefore, it will reduce the FE for H_2O_2 production. The electrooxidation process is more concerned with the electrochemical oxidation ability of anode materials, and no additional oxygen is needed to add in the cell. Thus, it

DOI: 10.1021/acs.est.9b04859
Environ. Sci. Technol. 2019, 53, 13878−13887

results in the low production of H_2O_2. Furthermore, the results suggest that the oxidation of tetracycline by M($^{\bullet}$OH) is fitted with pseudo-first-order kinetic reaction in all cases (inset in Figure 4b,c). Theoretically, M($^{\bullet}$OH) concentration is in a quasi-stationary state because they are very reactive and cannot be accumulated in the medium. It implies that the continuously generated M($^{\bullet}$OH) always reacted with tetracycline.[7]

$$O_2 + 2H^+ + 2e^- \rightarrow H_2O_2 \quad (3)$$

$$Fe^{2+} + H_2O_2 \rightarrow Fe^{3+} + OH^- + {}^{\bullet}OH \quad (4)$$

The effect of pH on tetracycline degradation by using the $Fe_{0.53}Co_{0.47}P$/NF anode is minimal as shown in Figure S18a. This further indicates that it is an electrooxidation process. It is different from the traditional electro-fenton process which will be affected by pH. Because natural wastewater has different conductivities, we evaluated the tetracycline removal efficiency at different electrolyte concentrations. Figure S18b reveals that the removal efficiency slightly decreased at reduced electrolyte concentration. To further validate the removal efficiency of tetracycline in low-salt and high-salt natural waters, we carried out simulation experiments with river water from Xiangjiang River (Hunan Province in China) and simulated seawater. The results suggested that tetracycline can be successfully removed by the $Fe_{0.53}Co_{0.47}P$/NF anode. Furthermore, the $Fe_{0.53}Co_{0.47}P$/NF anode shows the same superior TOC removal performance as the BDD anode (Figure S22a). The maximum TOC removal rates of 74.2 and 66% are obtained with the BDD anode and $Fe_{0.53}Co_{0.47}P$/NF anode after 8 h of electrooxidation at the current density of 12.5 mA cm^{-2}, respectively. Much low TOC removal rates of 32.5 and 48.5% are achieved with the Pt plate anode and NF anode under the same conditions, respectively, suggesting that these latter anodes have weak mineralization capacity for organic pollutants. Generally, the strong oxidizing ability of the $Fe_{0.53}Co_{0.47}P$/NF anode is mainly derived from the produced $^{\bullet}$OH or $^{\bullet}O_2^-$. Therefore, radical scavenger experiments are conducted to confirm which reactive radical plays a major role in the electrooxidation process. *tert*-Butanol and isopropanol are selected as scavengers to remove $^{\bullet}$OH. *p*-Benzoquinone and 4-hydroxy-2,2,6,6-tetramethylpiperidinyloxy (TEMPOL) are selected as scavengers to remove $^{\bullet}O_2^-$. As presented in Figure S19, the removal efficiency of the pollutant is slightly decreased with the addition of *p*-benzoquinone and TEMPOL. Particularly, the removal efficiencies are only 47 and 58% when isopropanol and *tert*-butanol are added. It demonstrates that $^{\bullet}$OH plays an important role in the electrooxidation process. Generally, the superoxide anion radical can be produced when oxygen obtains an electron in the cathode (reaction 5).[44] The superoxide anion radical can further generate H_2O_2 (reaction 6), and the produced H_2O_2 can react with Fe^{2+} released by $Fe_{0.53}Co_{0.47}P$/NF to produce homogeneous $^{\bullet}$OH (reaction 4), which can further oxidize tetracycline. Moreover, the standard reduction potential of the superoxide anion radical (−0.33 V vs NHE) is smaller than that of H_2O_2 (1.78 V vs NHE).[45] It means that H_2O_2 has stronger oxidation ability than the superoxide anion radical. However, the removal efficiency of tetracycline by H_2O_2 is less than 5% in our system (Figure S20). Therefore, tetracycline cannot be degraded by the superoxide anion radical because of the low oxidation ability. The superoxide anion radical can indirectly increase the production of $^{\bullet}$OH by generating H_2O_2, but it will not directly participate in the reaction to oxidize the organic pollutant. The concentration of ferrous ions released by $Fe_{0.53}Co_{0.47}P$/NF is low (Figure S16b). This leads to a low yield of $^{\bullet}$OH by the superoxide anion radical. Therefore, the removal efficiency of tetracycline is slightly decreased when TEMPOL and *p*-benzoquinone are added to remove the superoxide anion radical because the production of $^{\bullet}$OH is decreased. The production of $^{\bullet}$OH is mainly derived from anodic oxidation (reaction 1) in the electrooxidation process, and it can also be observed that the removal efficiency of tetracycline is greatly decreased when isopropanol and *tert*-butanol are added. Therefore, tetracycline is mainly degraded by $^{\bullet}$OH in the electrooxidation process.

$$O_2 + e^- \rightarrow {}^{\bullet}O_2^- \quad (5)$$

$$2O_2^- + 2H^+ \rightarrow O_2 + H_2O_2 \quad (6)$$

The $Fe_{0.53}Co_{0.47}P$/NF electrooxidation is also applied for the removal of other refractory organic pollutants. Dimethyl phthalate, one of refractory and toxic organic compounds, is chosen as the targeted contaminant. As presented in Figure S21, the high removal efficiencies of 71 and 69% are obtained with the BDD anode and $Fe_{0.53}Co_{0.47}P$/NF anode after 120 min of electrooxidation at the current density of 12.5 mA cm^{-2}, respectively. Much lower removal efficiency of 30% is achieved with the Pt anode under the same conditions. The corresponding MCE values for the trials of Figure 4c are given in Figure S22b. Similar high MCE values are obtained by both BDD and $Fe_{0.53}Co_{0.47}P$/NF anode because of the high TOC removal efficiencies achieved for both anodes. Both BDD and $Fe_{0.53}Co_{0.47}P$/NF anodes achieve nearly 80% of the MCE value at early electrooxidation, whereas lower MCE percentages of 47.5 and 23.75% are obtained with NF and Pt plate anodes, respectively. It further proves that $Fe_{0.53}Co_{0.47}P$/NF has high potential and effectiveness in the electrooxidation treatment of organic pollutants. Another important factor in anode comparison is the electrical energy consumption (EC). As shown in Figure S22c, the EC values are both high for the Pt plate and NF anode because of their smaller mineralization capacity. $Fe_{0.53}Co_{0.47}P$/NF and BDD anodes gave similar results. Therefore, it can be concluded that the $Fe_{0.53}Co_{0.47}P$/NF anode is an excellent substitute for the BDD anode in electrooxidation wastewater treatment. The stability of the activity of the $Fe_{0.53}Co_{0.47}P$/NF anode is also studied by cyclic experiments (Figure 4e). The results exhibited excellent removal efficiency for tetracycline even after five treatments, indicating a good stability of the $Fe_{0.53}Co_{0.47}P$/NF anode. The surface morphology and chemical state of the $Fe_{0.29}Co_{0.71}P$/NF anode after recycle experiments are conducted, and the results show that the surface morphology and chemical state of the catalyst are almost unchanged (Figures S23 and S24). Meanwhile, the reaction solution after first three cycles is also tested by inductively coupled plasma-optical emission spectrometry (Table S3). It can be found that the leakage of iron, cobalt, and phosphorus from the $Fe_{0.53}Co_{0.47}P$/NF anode is very low. These results further demonstrate that the $Fe_{0.53}Co_{0.47}P$/NF anode has high stability.

3.3. OER Activity of $Fe_{1-x}Co_xP$/NF. It is generally known that the reported OER activity of Fe-based electrocatalysts in acidic solution is much weaker than that in basic solution because they are instable and easily corroded in acidic condition.[46] The electrooxidation experiments of $Fe_{1-x}Co_xP$/NF are carried out in acidic solution (pH 5). Therefore, the

DOI: 10.1021/acs.est.9b04859
Environ. Sci. Technol. 2019, 53, 13878−13887

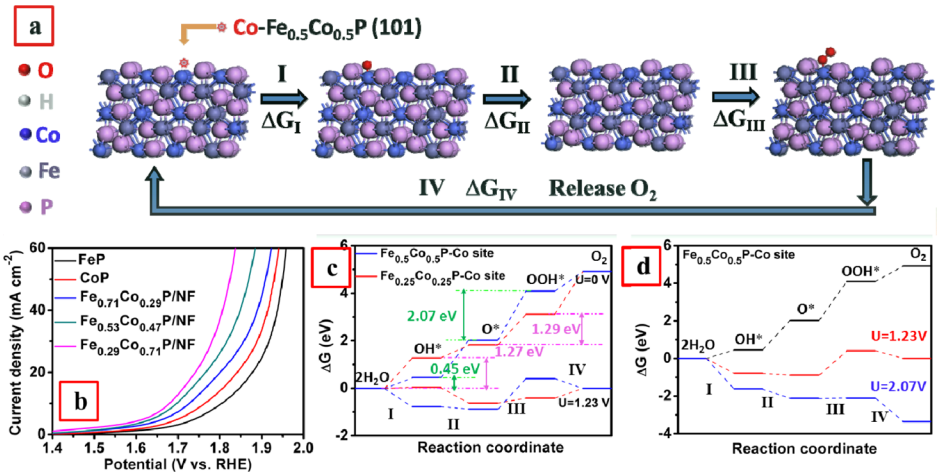

Figure 5. (a) Proposed 4e$^-$ mechanism of OER on $Fe_{0.25}Co_{0.75}P$ for DFT + U calculation. The Co site (*) in the (101) crystal plane was the active site; ΔG denotes the reaction Gibbs free energy, (b) LSV curves for $Fe_{0.29}Co_{0.79}P$/NF with a scan rate of 5 mV s^{-1} for OER under acidic conditions (pH = 5), (c) Gibbs free energy diagram of OER at U = 0 V and U = 1.23 V for $Fe_{0.25}Co_{0.75}P$ (Co site as the active site) and $Fe_{0.5}Co_{0.5}P$, and (d) Gibbs free energy diagram for elementary reactions of OER over $Fe_{0.5}Co_{0.5}P$.

electrocatalytic activity toward the OER of $Fe_{1-x}Co_xP$/NF is also studied in acidic solution to reveal the interrelation between electrooxidation and OER. $Fe_{1-x}Co_xP$/NFs are directly used as the binder-free working electrode in a three-electrode electrochemical system. As shown in Figure 5b, the $Fe_{0.29}Co_{0.71}P$/NF electrode exhibited excellent electrocatalytic activity toward OER with a lower overpotential (594 mV), which is much lower than that of $Fe_{0.71}Co_{0.29}P$/NF (679 mV), $Fe_{53}Co_{0.47}P$/NF (639 mV), bare CoP/NF (700 mV), and FeP/NF (720 mV) at the current density of 50 mA cm^{-2} (η_{50}), suggesting that $Fe_{0.29}Co_{0.71}P$/NF can catalyze the OER process with very high energy efficiency. These results further validate the previous hypothesis that the electrooxidation ability of $Fe_{53}Co_{0.47}P$/NF is higher than that of $Fe_{0.29}Co_{0.71}P$/NF because $Fe_{53}Co_{0.47}P$/NF has high OER overpotential and can produce more M(•OH) instead of O_2.

To further reveal the underlying mechanism, the DFT + U computations are used to analyze the overpotential and Gibbs free energy of reaction coordinate steps for OER based on the 4e$^-$ mechanism of water oxidation proposed by Norskov (see the Supporting Information for details).[47] The Co site played a crucial role in $Fe_{1-x}Co_xP$ for OER catalysis, and there are many Co sites with unsaturated coordination in the edge of layered bimetallic phosphide nanosheets. Therefore, the Co site in the (101) crystal plane is considered as the main active site of $Fe_{0.25}Co_{0.75}P$ and $Fe_{0.5}Co_{0.5}P$ for DFT + U computations. The corresponding $Fe_{0.5}Co_{0.5}P$ structures and proposed 4e$^-$ mechanism of water oxidation are shown in Figure 5a. The free energy diagrams of the reaction intermediates in the Gibbs free energy are displayed in Figure 5c. The intermediates, such as *OH, *O, and *OOH, are bound to the active site by oxygen with a single bond in consistent with the above-mentioned 4e$^-$ mechanism. The Gibbs free energy difference values of the first step of $Fe_{0.5}Co_{0.5}P$ (ΔG_I = 0.56 eV) is lower than that of $Fe_{0.25}Co_{0.75}P$ (ΔG_I = 1.27 eV), suggesting that $Fe_{0.25}Co_{0.75}P$ needs a smaller overpotential to drive water oxidation to produce hydroxyl radicals. Meanwhile, the Gibbs free energy difference values of the third step of $Fe_{0.5}Co_{0.5}P$ (ΔG_{III} = 2.07 eV) are higher than that of $Fe_{0.25}Co_{0.75}P$ (ΔG_{III} = 1.29 eV). It is also consistent with the higher calculated overpotential for $Fe_{0.5}Co_{0.5}P$ (0.84 V) (Figure 5d). This step is considered as the rate-determining step for the OER process, which is the same for these two electrocatalysts.[48,49] In other words, the lower barrier for the production of M(•OH) and higher barrier to generate O_2 means that $Fe_{0.5}Co_{0.5}P$ can produce more M(•OH) instead of O_2 compared with $Fe_{0.25}Co_{0.75}P$ under the same overpotential condition. These results also suggest that the electronic structure of $Fe_{0.5}Co_{0.5}P$ is modulated by Fe doping, which can optimize the adsorption energies of the OER intermediates. Therefore, Fe doping can modulate the electronic structure, increase the ECSA, and improve the electrical conductivity of $Fe_{0.5}Co_{0.5}P$, thereby resulting in the enhancement of electrooxidation ability. Moreover, it can also produce more M(•OH) instead of O_2 by appropriately regulating and controlling the mole ratio of Fe/Co and the voltage applied. The schematic diagram in Figure 4f explains the promotion effect of Fe doping in improving the adsorption and activation of water molecules for efficient production of M(•OH).

In this study, Fe doping is demonstrated to significantly improve the electrooxidation ability of $Fe_{0.53}Co_{0.47}P$ by rationally modifying the electron densities of catalytic sites. XPS and DFT calculation consistently elucidated that Fe doping can effectively optimize the electronic structure of $Fe_{0.53}Co_{0.47}P$. It makes Co positively charged and P negatively charged, which can promote water molecule adsorption and activation. This caused the $Fe_{0.53}Co_{0.47}P$ anode more likely to produce sorbed hydroxyl radicals to degrade pollutants. Moreover, unlike most conventional electro-fenton oxidation process that had strong pH limitations for organic removal, the prepared self-supported $Fe_{0.53}Co_{0.47}P$/NF anode exhibited superior removal efficiency of pollutants in all-pH conditions during the electrooxidation process. In summary, this study can shed new light on how to design advanced anode materials for electrooxidation and other applications.

■ ASSOCIATED CONTENT

Supporting Information

The Supporting Information is available free of charge on the ACS Publications website at DOI: 10.1021/acs.est.9b04859.

Theoretical calculation and other related analytical procedures (PDF)

DOI: 10.1021/acs.est.9b04859
Environ. Sci. Technol. 2019, 53, 13878−13887

AUTHOR INFORMATION

Corresponding Author

*E-mail: tanglin@hnu.edu.cn. Phone: +86-731-88822778. Fax: +86-731-88823701.

ORCID

Lin Tang: 0000-0001-6996-7955
Guangming Zeng: 0000-0002-4230-7647
Wangwang Tang: 0000-0001-7774-7493

Author Contributions

‖H.F. and J.Y. contribute equally to this article.

Notes

The authors declare no competing financial interest.

ACKNOWLEDGMENTS

This study was financially supported by Projects 51579096 and 51521006 supported by the National Natural Science Foundation of China, the Key Research and Development Project of Hunan Province of China (2017SK2241), the National Innovative Talent Promotion Program of China (2017RA2088), the Funds for Innovative Province Construction of Hunan Province of China (2019RS3012), and the National Program for Support of Top−Notch Young Professionals of China (2012).

REFERENCES

(1) Prieto-Rodríguez, L.; Oller, I.; Klamerth, N.; Agüera, A.; Rodríguez, E. M.; Malato, S. Application of solar AOPs and ozonation for elimination of micropollutants in municipal wastewater treatment plant effluents. *Water Res.* **2013**, *47*, 1521−1528.

(2) Zheng, J.; Su, C.; Zhou, J.; Xu, L.; Qian, Y.; Chen, H. Effects and mechanisms of ultraviolet, chlorination, and ozone disinfection on antibiotic resistance genes in secondary effluents of municipal wastewater treatment plants. *Chem. Eng. J.* **2017**, *317*, 309−316.

(3) Tang, L.; Liu, Y.; Wang, J.; Zeng, G.; Deng, Y.; Dong, H.; Feng, H.; Wang, J.; Peng, B. Enhanced activation process of persulfate by mesoporous carbon for degradation of aqueous organic pollutants: Electron transfer mechanism. *Appl. Catal., B* **2018**, *231*, 1−10.

(4) Yao, W.; Wang, X.; Yang, H.; Yu, G.; Deng, S.; Huang, J.; Wang, B.; Wang, Y. Removal of pharmaceuticals from secondary effluents by an electro-peroxone process. *Water Res.* **2016**, *88*, 826−835.

(5) Zhang, R.; Yang, Y.; Huang, C.-H.; Zhao, L.; Sun, P. Kinetics and modeling of sulfonamide antibiotic degradation in wastewater and human urine by UV/H_2O_2 and UV/PDS. *Water Res.* **2016**, *103*, 283−292.

(6) Sirés, I.; Brillas, E.; Oturan, M. A.; Rodrigo, M. A.; Panizza, M. Electrochemical advanced oxidation processes: today and tomorrow. A review. *Environ. Sci. Pollut. Res.* **2014**, *21*, 8336−8367.

(7) Oturan, M. A.; Aaron, J.-J. Advanced Oxidation Processes in Water/Wastewater Treatment: Principles and Applications. A Review. *Crit. Rev. Environ. Sci. Technol.* **2014**, *44*, 2577−2641.

(8) Martínez-Huitle, C. A.; Brillas, E. Decontamination of wastewaters containing synthetic organic dyes by electrochemical methods. An updated review. *Appl. Catal., B* **2009**, *87*, 105−145.

(9) García-Montoya, M. F.; Gutiérrez-Granados, S.; Alatorre-Ordaz, A.; Galindo, R.; Ornelas, R.; Peralta-Hernández, J. M. Application of electrochemical/BDD process for the treatment wastewater effluents containing pharmaceutical compounds. *J. Ind. Eng. Chem.* **2015**, *31*, 238−243.

(10) Panizza, M.; Giacomo, C. Direct and mediated anodic oxidation of organic pollutants. *Chem. Rev.* **2009**, *109*, 6541.

(11) Yang, H.; Zhang, Y.; Hu, F.; Wang, Q. Urchin-like CoP Nanocrystals as Hydrogen Evolution Reaction and Oxygen Reduction Reaction Dual-Electrocatalyst with Superior Stability. *Nano Lett.* **2015**, *15*, 7616.

(12) Liu, Q.; Tian, J.; Cui, W.; Jiang, P.; Cheng, N.; Asiri, A. M.; Sun, X. Carbon nanotubes decorated with CoP nanocrystals: a highly active non-noble-metal nanohybrid electrocatalyst for hydrogen evolution. *Angew. Chem., Int. Ed.* **2014**, *126*, 6828−6832.

(13) Deng, Y.; Tang, L.; Feng, C.; Zeng, G.; Wang, J.; Zhou, Y.; Liu, Y.; Peng, B.; Feng, H. Construction of plasmonic Ag modified phosphorous-doped ultrathin g-C_3N_4 nanosheets/$BiVO_4$ photocatalyst with enhanced visible-near-infrared response ability for ciprofloxacin degradation. *J. Hazard. Mater.* **2018**, *344*, 758−769.

(14) Wang, J.; Tang, L.; Zeng, G.; Deng, Y.; Liu, Y.; Wang, L.; Zhou, Y.; Guo, Z.; Wang, J.; Zhang, C. Atomic scale g-C_3N_4 /$Bi_2WO_6$2D/2D heterojunction with enhanced photocatalytic degradation of ibuprofen under visible light irradiation. *Appl. Catal., B* **2017**, *209*, 285−294.

(15) Tang, L.; Feng, H.; Tang, J.; Zeng, G.; Deng, Y.; Wang, J.; Liu, Y.; Zhou, Y. Treatment of arsenic in acid wastewater and river sediment by Fe@Fe_2O_3 nanobunches: The effect of environmental conditions and reaction mechanism. *Water Res.* **2017**, *117*, 175.

(16) Deng, Y.; Tang, L.; Zeng, G.; Zhu, Z.; Yan, M.; Zhou, Y.; Wang, J.; Liu, Y.; Wang, J. Insight into highly efficient simultaneous photocatalytic removal of Cr(VI) and 2,4-diclorophenol under visible light irradiation by phosphorus doped porous ultrathin g-C 3 N 4 nanosheets from aqueous media: Performance and reaction mechanism. *Appl. Catal., B* **2017**, *203*, 343−354.

(17) Tang, L.; Yang, G.-D.; Zeng, G.-M.; Cai, Y.; Li, S.-S.; Zhou, Y.-Y.; Pang, Y.-Y.; Zhang, Y.; Luna, B. Synergistic effect of iron doped ordered mesoporous carbon on adsorption-coupled reduction of hexavalent chromium and the relative mechanism study. *Chem. Eng. J.* **2014**, *239*, 114−122.

(18) Xue, Z.-H.; Su, H.; Yu, Q.-Y.; Zhang, B.; Wang, H.-H.; Li, X.-H.; Chen, J.-S. Janus Co/CoP Nanoparticles as Efficient Mott−Schottky Electrocatalysts for Overall Water Splitting in Wide pH Range. *Adv. Energy Mater.* **2017**, *7*, 1602355.

(19) Liang, H.; Gandi, A. N.; Anjum, D. H.; Wang, X.; Schwingenschlögl, U.; Alshareef, H. N. Plasma-Assisted Synthesis of NiCoP for Efficient Overall Water Splitting. *Nano Lett.* **2016**, *16*, 7718−7725.

(20) Zhang, B.; Lui, Y. H.; Gaur, A. P. S.; Chen, B.; Tang, X.; Qi, Z.; Hu, S. Hierarchical FeNiP @ Ultrathin Carbon Nanoflakes as Alkaline Oxygen Evolution and Acidic Hydrogen Evolution Catalyst for Efficient Water Electrolysis and Organic Decomposition. *ACS Appl. Mater. Interfaces* **2018**, *10*, 8739−8748.

(21) Wang, Z.; He, H.; Lai, X. High precision control technique for constant current regulation in primary-side regulation systems. *Electron. Lett.* **2014**, *50*, 1870−1872.

(22) Kresse, G.; Hafner, J. Ab initio molecular dynamics for liquid metals. *Phys. Rev. B: Condens. Matter Mater. Phys.* **1993**, *48*, 13115−13118.

(23) Oba, F.; Togo, A.; Tanaka, I.; Paier, J.; Kresse, G. Defect energetics in ZnO: A hybrid Hartree-Fock density functional study. *Phys. Rev. B: Condens. Matter Mater. Phys.* **2008**, *77*, 245202.

(24) Ling, Y.; Wang, Z.; Wang, Z.; Peng, R.; Lin, B.; Yu, W.; Isimjan, T. T.; Lu, Y. A robust carbon tolerant anode for solid oxide fuel cells. *Sci. China Mater.* **2015**, *58*, 204−212.

(25) Perdew, J. P.; Burke, K.; Ernzerhof, M. Generalized Gradient Approximation Made Simple. *Phys. Rev. Lett.* **1996**, *77*, 3865−3868.

(26) Han, A.; Huanlin, C.; Zijun, S.; Jun, X.; Pingwu, D. High catalytic activity for water oxidation based on nanostructured nickel phosphide precursors. *Chem. Commun.* **2015**, *51*, 11626−11629.

(27) Stern, L.-A.; Feng, L.; Song, F.; Hu, X. Ni_2P as a Janus catalyst for water splitting: the oxygen evolution activity of Ni_2P nanoparticles. *Energy Environ. Sci.* **2015**, *8*, 2347−2351.

(28) Liang, H.; Gandi, A. N.; Anjum, D. H.; Wang, X.; Schwingenschlögl, U.; Alshareef, H. N. Plasma-Assisted Synthesis of NiCoP for Efficient Overall Water Splitting. *Nano Lett.* **2016**, *16*, 7718−7725.

(29) Yang, F.; Chen, Y.; Cheng, G.; Chen, S.; Luo, W. An Ultrathin Nitrogen-Doped Carbon Coated with CoP for Efficient Hydrogen Evolution. *ACS Catal.* **2017**, *7*, 3824−3831.

DOI: 10.1021/acs.est.9b04859
Environ. Sci. Technol. 2019, 53, 13878−13887

(30) Cook, T. R.; Dogutan, D. K.; Reece, S. Y.; Surendranath, Y.; Teets, T. S.; Nocera, D. G. Solar energy supply and storage for the legacy and nonlegacy worlds. *Chem. Rev.* **2010**, *110*, 6474−6502.
(31) Petrykin, V.; Macounova, K.; Shlyakhtin, O. A.; Krtil, P. Tailoring the Selectivity for Electrocatalytic Oxygen Evolution on Ruthenium Oxides by Zinc Substitution. *Angew. Chem., Int. Ed.* **2010**, *49*, 4813−4815.
(32) Jiang, P.; Liu, Q.; Liang, Y.; Tian, J.; Asiri, A. M.; Sun, X. A cost-effective 3D hydrogen evolution cathode with high catalytic activity: FeP nanowire array as the active phase. *Angew. Chem.* **2015**, *126*, 13069−13073.
(33) Fan, X.; Liu, Y.; Chen, S.; Shi, J.; Wang, J.; Fan, A.; Zan, W.; Li, S.; Goddard, W. A.; Zhang, X.-M. Defect-enriched iron fluoride-oxide nanoporous thin films bifunctional catalyst for water splitting. *Nat. Commun.* **2018**, *9*, 1809.
(34) Long, X.; Li, G.; Wang, Z.; Zhu, H.; Zhang, T.; Xiao, S.; Guo, W.; Yang, S. Metallic Iron-Nickel Sulfide Ultrathin Nanosheets As a Highly Active Electrocatalyst for Hydrogen Evolution Reaction in Acidic Media. *J. Am. Chem. Soc.* **2015**, *137*, 11900−11903.
(35) Xin, H.; Vojvodic, A.; Voss, J.; Nørskov, J. K.; Abild-Pedersen, F. Effects of d-band shape on the surface reactivity of transition-metal alloys. *Phys. Rev. B: Condens. Matter Mater. Phys.* **2014**, *89*, 867−875.
(36) Acerbi, N.; Tsang, S. C. E.; Jones, G.; Golunski, S.; Collier, P. Rationalization of Interactions in Precious Metal/Ceria Catalysts Using the d-Band Center Model. *Angew. Chem., Int. Ed.* **2013**, *52*, 7737−7741.
(37) Hammer, B.; Nørskov, J. K. Erratum to Electronic factors determining the reactivity of metal surfaces. *Surf. Sci.* **1996**, *359*, 306.
(38) Wu, Y.; Liu, X.; Han, D.; Song, X.; Shi, L.; Song, Y.; Niu, S.; Xie, Y.; Cai, J.; Wu, S. Electron density modulation of $NiCo_2S_4$ nanowires by nitrogen incorporation for highly efficient hydrogen evolution catalysis. *Nat. Commun.* **2018**, *9*, 1425.
(39) Murugananthan, M.; Yoshihara, S.; Rakuma, T.; Uehara, N.; Shirakashi, T. Electrochemical degradation of 17β-estradiol (E2) at boron-doped diamond (Si/BDD) thin film electrode. *Electrochim. Acta* **2007**, *52*, 3242−3249.
(40) Ganiyu, S. O.; Oturan, N.; Raffy, S.; Cretin, M.; Esmilaire, R.; van Hullebusch, E.; Esposito, G.; Oturan, M. A. Sub-stoichiometric titanium oxide (Ti_4O_7) as a suitable ceramic anode for electro-oxidation of organic pollutants: A case study of kinetics, mineralization and toxicity assessment of amoxicillin. *Water Res.* **2016**, *106*, 171−182.
(41) Yang, L.; Yu, J.; Wei, Z.; Li, G.; Cao, L.; Zhou, W.; Chen, S. Co-N-doped MoO_2 nanowires as efficient electrocatalysts for the oxygen reduction reaction and hydrogen evolution reaction. *Nano Energy* **2017**, *41*, 772−779.
(42) Zhou, W.; Lu, J.; Zhou, K.; Yang, L.; Ke, Y.; Tang, Z.; Chen, S. $CoSe_2$ nanoparticles embedded defective carbon nanotubes derived from MOFs as efficient electrocatalyst for hydrogen evolution reaction. *Nano Energy* **2016**, *28*, 143−150.
(43) Yang, L.; Zhou, W.; Lu, J.; Hou, D.; Ke, Y.; Li, G.; Tang, Z.; Kang, X.; Chen, S. Hierarchical spheres constructed by defect-rich MoS_2/carbon nanosheets for efficient electrocatalytic hydrogen evolution. *Nano Energy* **2016**, *22*, 490−498.
(44) Huang, L.-Z.; Zhu, M.; Liu, Z.; Wang, Z.; Hansen, H. C. B. Single sheet iron oxide: An efficient heterogeneous electro-Fenton catalyst at neutral pH. *J. Hazard. Mater.* **2019**, *364*, 39−47.
(45) Khan, H.; Rigamonti, M. G.; Patience, G. S.; Boffito, D. C. Spray dried TiO_2/WO_3 heterostructure for photocatalytic applications with residual activity in the dark. *Appl. Catal., B* **2018**, *226*, 311−323.
(46) Lu, J.; Xiong, T.; Zhou, W.; Yang, L.; Tang, Z.; Chen, S. Metal Nickel Foam as an Efficient and Stable Electrode for Hydrogen Evolution Reaction in Acidic Electrolyte under Reasonable Over-potentials. *ACS Appl. Mater. Interfaces* **2016**, *8*, 5065.
(47) Li, P.; Duan, X.; Kuang, Y.; Li, Y.; Zhang, G.; Liu, W.; Sun, X. Tuning Electronic Structure of NiFe Layered Double Hydroxides with Vanadium Doping toward High Efficient Electrocatalytic Water Oxidation. *Adv. Energy Mater.* **2018**, *8*, 1703341.
(48) Jia, Y.; Zhang, L.; Du, A.; Gao, G.; Chen, J.; Yan, X.; Brown, C. L.; Yao, X. Defect Graphene as a Trifunctional Catalyst for Electrochemical Reactions. *Adv. Mater.* **2016**, *28*, 9532−9538.
(49) Li, T.; Lv, Y.; Su, J.; Wang, Y.; Yang, Q.; Zhang, Y.; Zhou, J.; Xu, L.; Sun, D.; Tang, Y. Anchoring $CoFe_2O_4$ Nanoparticles on N-Doped Carbon Nanofibers for High-Performance Oxygen Evolution Reaction. *Adv. Sci.* **2017**, *4*, 1700226.

DOI: 10.1021/acs.est.9b04859
Environ. Sci. Technol. 2019, 53, 13878−13887